water

MDPI

Article

Numerical Study of the Cavitation Performance of an Ice-Blocked Propeller Considering the Free Surface Effect

Li Zhou [1,2], Anwen Zhang [3], Shifeng Ding [2,*], Sen Han [3], Fang Li [1,2] and Pentti Kujala [2,4]

[1] State Key Laboratory of Ocean Engineering, Shanghai Jiao Tong University, Shanghai 200240, China; zhouli209@sjtu.edu.cn (L.Z.); fang.li@sjtu.edu.cn (F.L.)
[2] School of Ocean and Civil Engineering, Shanghai Jiao Tong University, Shanghai 200240, China; pentti.kujala@aalto.fi
[3] School of Naval Architecture and Ocean Engineering, Jiangsu University of Science and Technology, Zhenjiang 212003, China; 221210101325@stu.just.edu.cn (A.Z.); hansen@just.edu.cn (S.H.)
[4] School of Engineering, Aalto University, 02150 Espoo, Finland
* Correspondence: 15001945469@163.com; Tel.: +86-15001945469

Abstract: Propeller cavitation performance can be predicted based on model tests or simulations. However, the cavitation performance of an ice-blocked propeller near the free surface differs from that of a propeller in the cavitation tunnel. Therefore, research on the cavitation performance simulation of propellers near the free surface holds crucial scientific significance. In this study, a coupled model was established using Computational Fluid Dynamics (CFD) and the Volume of Fluid (VOF) coupling method. The CFD-VOF model weighted the overlapping grids and simulated the cavitation performance of an ice-blocked propeller using various immersion depths, cavitation numbers, and advance coefficients. The propeller inflow ahead of the propeller and the wake field behind it were controlled to accurately obtain the propeller cavitation performance. Moreover, a comparison was conducted between the cavitation tunnel test results and the numerical simulation results at various immersion depths. When the immersion depth was at a distance of 1*D*, the effect of the free surface on the propeller cavitation performance became significant. When the immersion depth was at a distance of 9*D*, the average errors between the numerical simulation and the model test data were within 10%. This study analyzed the cavitation performance of ice-blocked propellers near the free surface and provided valuable insights for the design of ice-class propellers.

Keywords: propeller; cavitation; free surface; ice blockage; polar ship

check for updates

Citation: Zhou, L.; Zhang, A.; Ding, S.; Han, S.; Li, F.; Kujala, P. Numerical Study of the Cavitation Performance of an Ice-Blocked Propeller Considering the Free Surface Effect. *Water* **2024**, *16*, 3260. https://doi.org/10.3390/w16223260

Academic Editor: Hung Tao Shen

Received: 26 September 2024
Revised: 9 November 2024
Accepted: 11 November 2024
Published: 13 November 2024

Copyright: © 2024 by the authors. Licensee MDPI, Basel, Switzerland. This article is an open access article distributed under the terms and conditions of the Creative Commons Attribution (CC BY) license (https://creativecommons.org/licenses/by/4.0/).

1. Introduction

Polar icebreakers play a pivotal role when confronted with the extreme cold and thick ice cover of polar regions. They provide essential support for resource exploration, trade, and scientific research. The icebreaking performance of polar icebreakers depends on various factors, with particular attention given to the impact of cavitation on propeller efficiency [1]. The cavitation performance of the propeller near the free surface is affected by ice blockage and the free surface. Ice blockage and the free surface challenge the detection of propeller cavitation phenomena. The cavitation tunnel model tests can be utilized to investigate the effect of ice blockages on the cavitation performance of propellers; however, these tests do not account for the presence of a free surface [2]. However, the cavitation performance of ice-blocked propellers near the free surface at various immersion depths requires investigation using a new coupled model [3]. Hence, employing the CFD-VOF model to capture the free surface contributes to the analysis of the effect of ice blockages and the free surface on propeller cavitation performance. Furthermore, it is possible to obtain the effect of the free surface on ice-blocked propeller cavitation performance using various immersion depths, cavitation numbers, and advance coefficients. Furthermore, as

Arctic routes have become navigable, the study of polar propeller cavitation performance based on computational fluid dynamics is currently under active research.

The computation of the cavitation performance of near-surface propellers can generally be divided into several components. These include the ice blockage, the inflow field in front of the propeller and the wake field behind it, the free surface fluctuation, the immersion depth, and the propeller's hydrodynamic performance.

In order to simulate the effect of the ice blockage on the cavitation performance of the propeller, researchers have conducted a comparative study between experimental and numerical investigations of propeller ice blockages in cavitation flows. The effect of the distance between the ice and the propeller was analyzed. Zhou et al. performed ice-blocked propeller experiments within a cavitation tunnel at the China Ship Research Center. Their study revealed that the interaction between the ice blockage and propeller cavitation has a combined effect on the propeller hydrodynamic performance [4]. Ebrahimi et al. conducted model tests of propeller hydrodynamic performance and cavitation inception in a cavitation tunnel and demonstrated that the cavitation significantly impacts the propeller's hydrodynamic performance. Their research also highlighted that this performance is affected by factors such as propeller shapes, the operational environment, motion, etc. [5]. Khan et al. developed a novel numerical tool to evaluate the impact of propeller-ice interactions on the forces exerted on the propellers. Their simulation results confirmed an inverse proportionality between the ice blockage effect and the distance between the ice and the propeller. When the distance is small or the ice-propeller is in direct contact, the ice blockage effect significantly impacts the propeller hydrodynamic performance [6].

In order to study the inflow field in front of the propeller and the wake field behind the propeller, Viitanen et al. utilized a marine propeller subjected to oblique inflow conditions to simulate unsteady cavitation phenomena. They further investigated the pressure fluctuations on the propeller blades and in the wake region caused by the dynamic cavitation structures [7]. Baek et al. investigated the effect of the advance coefficient on the propeller wake, which could offer insight into developing reliable wake modeling techniques [8]. Meng et al. proposed that the hydrodynamic excitation generated by the rotation of the propeller in non-uniform inflow results in propulsion shaft vibration, which feeds back to the hydrodynamics of the propeller, leading to the bidirectional coupling of the propeller-shaft system [9]. Hou and Hu investigated the impact of the axial inflow velocity and the skewed inflow incidence angle on the propeller hydrodynamic performance. Both the inflow ahead of the propeller and the wake behind the propeller affect the propeller hydrodynamic performance through the influence of non-uniform flow within the flow field; this effect is significant and cannot be ignored [10].

In order to simulate the fluctuation of the free surface and the effect of the free surface on the propeller's cavitation performance at different immersion depths, Guo et al. studied the hydrodynamic performance of propellers in waves using an experimental approach. They compared the propulsive efficiency of the propeller under two conditions: open water and waves, as well as its performance at different immersion depths. They proposed reasonable methods to avoid reducing propeller efficiency [11]. Califano and Steen utilized the Reynolds-Averaged Navier-Stokes (RANS) method to investigate the hydrodynamic performance of propellers near the free surface. They discovered that during the propeller rotation, there are periodic oscillations in thrust and torque compared to situations without a free surface [12]. Tokgoz et al. applied the RANS method to study the fluctuation in the thrust of propellers in waves at different immersion depths and under advance coefficient conditions. They found that for larger immersion depths, the numerical results matched well with experimental data, whereas for shallower immersion depths the difference was more significant [13]. Chen et al. utilized the Boundary Element Method (BEM) to assess the convergence of the Finite Volume Method (FVM) [14]. Their research employed the FVM to examine the influence of various geometrical inflow conditions on the hydrodynamic performance and noise characteristics of six-bladed propellers. Their study highlights that

the free surface fluctuations are dependent on the immersion depth, and when the propeller is immersed to a certain depth, the fluctuation of the free surface can be neglected.

For the simulations of the propeller's hydrodynamic performance, Jin et al. introduced a coupled approach utilizing the Boundary Element Method and Reynolds-Averaged Navier-Stokes (BEM-RANS) for assessing the performance of ducted propellers. This methodology analyzes the effects of different upstream surfaces by forecasting the resulting effective wake [15]. Liu et al. utilized the RANS model to simulate tip vortex flow and cavitation. They conducted a comparison of two turbulence models with experimental data, analyzing the excessive dissipation caused by these models. Turbulence is recognized as a key source term in the energy transport equation [16]. In this paper, this research utilizes a CFD-VOF coupled model to investigate the cavitation performance of propellers. It accurately simulates the effects of ice blockages on cavitation performance while also assessing the effect of the free surface at different immersion depths. This approach closely reflects the actual operational conditions of propellers.

Although there has been extensive research on the effect of the free surface on a propeller's hydrodynamic performance, there is currently a lack of research on the aspect of propeller cavitation performance. To investigate the cavitation performance of ice-blocked propellers near the free surface, this paper simulated the free surface using the VOF method and controlled the inflow ahead of the propeller and the wake behind the propeller. Numerical simulations were conducted using a fixed-spacing ice-propeller distance model and cavitation model, with the establishment of boundary conditions, and the propeller was positioned at different immersion depths by adjusting its location along the *Z*-axis. Finally, the propeller thrust and torque under different simulation conditions were analyzed. The effect of cavitation caused by ice blockages near the free surface on the propeller hydrodynamic performance was summarized.

2. Numerical Simulation Methods

2.1. Governing Equations

In the spatial coordinate system $O \rightarrow xyz$, the description of the fluid flow around the propeller is defined with the coordinate origin O located at the center of propeller rotation. The x-axis represents the inflow direction (bow of the ship), the y-axis corresponds to starboard, and the z-axis is oriented vertically downward, as illustrated in Figure 1.

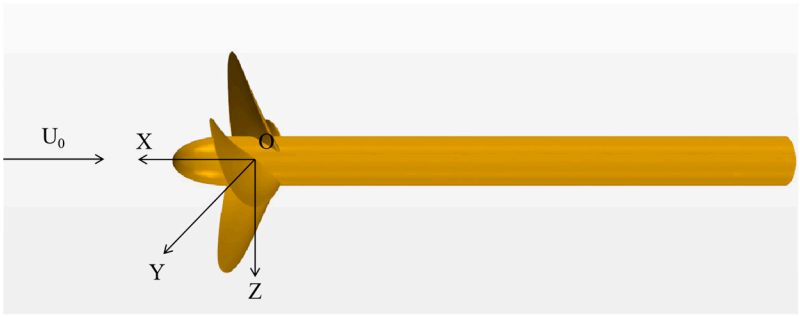

Figure 1. Flow control.

The rotational speed of ship propellers is typically low, and the surrounding fluid flow can be approximated as an incompressible viscous fluid. The RANS equations, which are applicable to viscous fluid dynamics, are employed to analyze variations in propeller performance [17]. Additionally, due to the limited heat exchange during the propeller motion, terms related to heat transfer can be neglected when solving the continuity and momentum conservation equations, which take the following form:

$$\frac{\partial U_i}{\partial x_i} = 0 \tag{1}$$

$$\frac{\partial U_i}{\partial t} + \frac{\partial U_i U_j}{\partial x_j} = f_i - \frac{1}{\rho}\frac{\partial p}{\partial x_i} + \frac{\partial p}{\partial x_j}(v(\frac{\partial U_i}{\partial x_j} + \frac{\partial U_j}{\partial x_i}) - \overline{U'_i U'_j}) \tag{2}$$

where x_i, x_j are independent coordinates; U_i, U_j are Reynolds-averaged velocity components; f_i signifies the unit mass volume force; ρ is fluid density; p is pressure; ν is fluid viscosity; $-\rho U'_i U'_j$ is Reynolds stress; t is time.

Based on the Bousinesq assumption, the Reynolds stress can be expressed as follows:

$$-U'_i U'_j = v_t(\frac{\partial U_i}{\partial x_j} + \frac{\partial U_j}{\partial x_i}) - \frac{2}{3}\delta_{ij}k \tag{3}$$

where v_t represents eddy viscosity; k denotes turbulent kinetic energy; δ_{ij} is Kronecker delta.

In the calculations, the SST K-ω turbulence model is employed to estimate the eddy viscosity.

2.2. Free Surface Control

The VOF model [18] is employed to track the free surface. This model is primarily applied in the study of two or more immiscible fluids and utilizes volume fractions to weigh the different fluids. The fluid volume fraction, denoted as α, satisfies the following equation:

$$\alpha(\vec{x}, t) = \begin{cases} 1, \vec{x} \in V_1 \\ 0, \vec{x} \in V_2 \end{cases} \tag{4}$$

For an individual grid cell, if $\alpha = 0$, then the grid unit is occupied by water; if $0 < \alpha < 1$, then the grid unit is occupied by water and air. The fluid density and viscosity coefficients in the equation are calculated by:

$$\begin{cases} \rho = \alpha(\vec{x}, t)\rho_a + (1 - \alpha(\vec{x}, t))\rho_w \\ \mu = \alpha(\vec{x}, t)\mu_a + (1 - \alpha(\vec{x}, t))\mu_w \end{cases} \tag{5}$$

where w is water; a is air.

2.3. Numerical Wave Generation and Absorption

At the velocity inlet boundary, numerical wave generation is performed using linear wave theory, where the inflow velocity is the linear superposition of the inlet velocity and wave speed [19].

$$u_w = -A\omega_0 \frac{coshk_w(h-z)}{sinhk_w h} sin(\omega_e t + k_w x) \tag{6}$$

$$v_w = 0 \tag{7}$$

$$\omega_w = -A\omega_0 \frac{coshk_w(h-z)}{sinhk_w h} cos(\omega_e t + k_w x) \tag{8}$$

where h denotes the water depth; k_w represents the wave number; A is the wave amplitude; $\omega_e = \omega_0 + k_w u_0$ signifies the encounter frequency; u_0 is the ship speed; ω_0 is the intrinsic wave frequency.

The wave profile is expressed as follows:

$$\zeta = A\omega_0 sin(\omega_e t + k_w x) \tag{9}$$

To ensure computational accuracy and simulate real-world conditions, wave absorption (eliminating reflected waves) is necessary at the stern of the vessel, where the RANS equations include $f_i \neq 0$ within the wave damping region.

$$f_i = (0, 0d(x)W) \tag{10}$$

$$d(x) = \begin{cases} \alpha(x_s - x), x \leq x_s \\ 0, \qquad\quad x > x_s \end{cases} \tag{11}$$

where α is the wave damping coefficient; x_s is the starting position of the wave damping region.

2.4. Cavitation Coefficient

The pressure conditions of the model tests are similar to the cavitation number [20]. The flow cavitation number σ_v and the rotational cavitation number σ_n are defined as follows:

$$\sigma_v = \frac{P - P_v}{\frac{1}{2}\rho V^2}$$

$$\sigma_n = \frac{P - P_v}{\frac{1}{2}\rho (nD)^2}$$

where P is the pressure of the shaft center, P_v is the saturated vapor pressure.

The thrust coefficient K_T, torque coefficient K_Q, and propeller efficiency η_0 are defined as follows:

$$J = \frac{V}{nD}$$

$$K_T = \frac{T}{\rho n^2 D^4}$$

$$K_Q = \frac{Q}{\rho n^2 D^5}$$

$$\eta_0 = \frac{JK_T}{2\pi K_Q}$$

where V represents the flow velocity, n denotes the propeller rotational speed, D is the diameter of the propeller, T indicates the thrust produced by the propeller, Q is the torque exerted by the propeller, and ρ signifies the density of water.

To facilitate reference and readability, commonly used abbreviations and symbols are compiled in Table 1.

Table 1. List of Symbols.

D	propeller diameter	ζ	wave crest elevation	ν	fluid viscosity	n	rotation speed
H	distance of propeller-surface	α	wave damping coefficient	ρ	fluid density	P	pressure
w	water	J	advance coefficient	ω_0	intrinsic wave frequency	A	wave amplitude
a	air	σ_n	cavitation number	x_s	starting position of the wave damping region	k_w	wave number
L	distance of propeller-ice	h	water depth	ω_e	encounter frequency	u_0	ship speed
V	flow velocity	T	propeller thrust	Q	propeller torque	P_v	saturated vapor pressure

3. Numerical Setup

3.1. Geometric Model

The propeller model used in the numerical simulations is the same as the one employed in the cavitation tunnel experiments, as illustrated in Figure 2. The propeller is scaled at 1:28 and constructed from aluminum alloy, rotating in a right-handed direction.

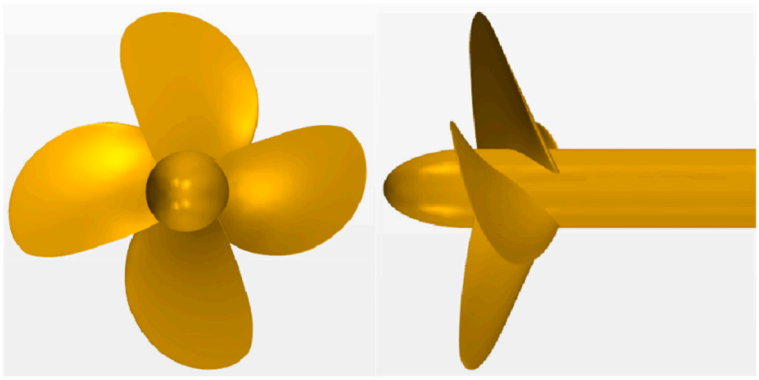

Figure 2. Computational model of the propeller.

When ships navigate in brash ice channels, the suction effect of the propeller causes the brash ice to be drawn into the propeller inflow field. Ship resistance and propeller ice blockage result in higher propulsion power requirements compared to operations in open water [21]. To realistically simulate the ice blockage condition for the propeller, an ice blockage was installed in the inflow field. The ice blockage model was represented as a regular rectangular block that is insoluble in water, with dimensions of 430 mm in length, 250 mm in width, and 125 mm in height. Considering that the ice-propeller spacing is $L/D = 0.15$, the propeller performance is at its worst. In this particular case, this paper conducted a study on the propeller cavitation performance near the free surface under ice blockage conditions. The model of propeller-ice spacing was built in STAR-CCM+, as shown in Figure 3.

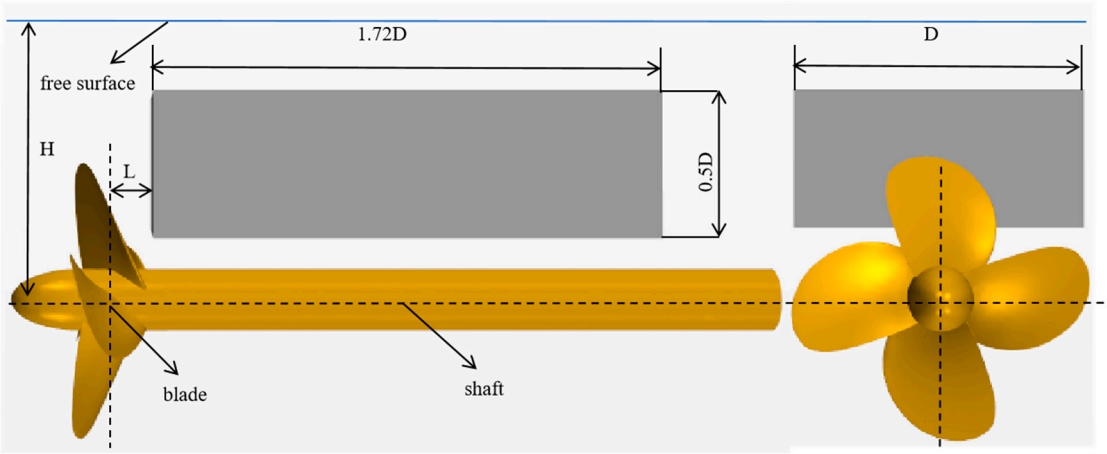

Figure 3. The schematic of the spacing and arrangement between ice and the propeller.

3.2. Computational Domain and Mesh

To precisely simulate the propeller cavitation performance near the water surface, the computational domain for the numerical simulation is depicted in Figure 4. The computational domain is structured as a rectangular prism, 10 m in length, 8 m in width, and 7 m in height. The distance from the center of the propeller shaft to the inlet of the inflow and the outlet of the pressure is 5 m, precisely controlling the inflow ahead of the propeller and the wake behind it. The portion above the water surface consists of 2 m of air and 5 m of liquid to accurately account for the effect of the free surface. The direction of the static water wave and inflow is from the inflow inlet to the pressure outlet. The rotating propeller is simulated using overlapping grids. The computational domain was divided into a far-field station region and a near-field rotation region. To analyze the difference between the propeller within the cavitation tunnel and near the water surface, this paper primarily conducted numerical simulations of the propeller cavitation performance at

different immersion depths. In comparison to the cavitation tunnel section, the boundary conditions for the computational domain of the propeller near the water surface were set as follows: the propeller blades, shaft, and ice block surfaces were set as smooth walls. An overlapping grid interface was created on the surface of the cylindrical region in the rotation region, coupling the grids of the rotation region with those of the station region. The boundary conditions for the sides, top, and bottom of the computational domain were defined as velocity inlets, and the outlet was configured as a pressure outlet. The surface of the propeller was set as a smooth wall. For capturing water surface fluctuations, a static water wave approach was employed. Furthermore, the Multiple Reference Frames method (MRF) [22] was utilized to simulate the propeller cavitation performance.

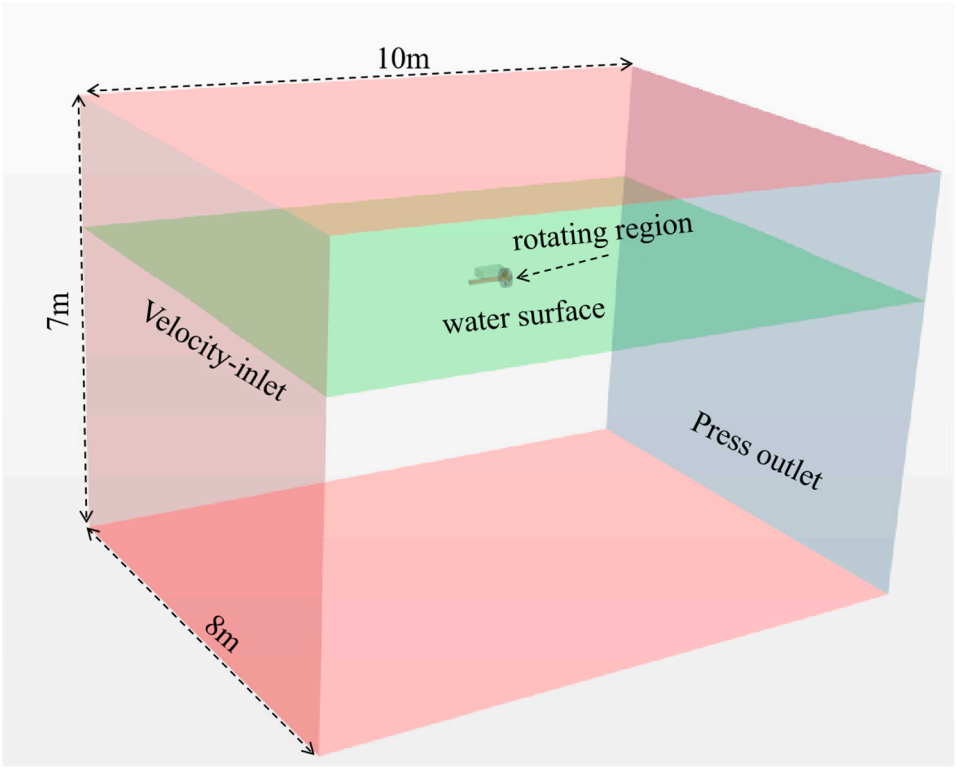

Figure 4. The computational domain.

The simulation domain is partitioned into a stationary region and a rotating region. The volume mesh of the computational domain employs a structured mesh, and the boundary layer mesh uses a prismatic layer mesh. The propeller utilizes a refined mesh with an automated surface repair process. The grids of the rotation and static regions are generated with an appropriate growth rate. The final mesh count is 3.89 million, with 0.78 million in the rotating region and 3.11 million in the stationary region. To ensure the geometric details of the propeller, the surface prismatic layer mesh of the propeller is set to 15 layers, with an appropriate prismatic layer thickness chosen. The mesh in the rotation region is refined to ensure that the wall Y+ is less than 1 at any position on the surface of the propeller and the shaft under full immersion conditions. Figure 5 depicts the surface mesh of the propeller along with the wall Y+ values. Figure 6 illustrates the mesh in the rotation and some of the static regions. "Figure 6A" and "Figure 6B" denote mesh refinement in the inflow and wake fields, respectively. "Figure 6C" represents mesh refinement in the water surface region for better capture of water surface fluctuations. "Figure 6D" signifies the overlapping region and the ice block, where the ice block is situated in the static region, and both the propeller and shaft employ refined meshes. A grid transition is implemented between the ice block and the propeller. "Figure 6E" presents a cross-sectional view of the rotation region of the propeller blade. The entire simulation domain mesh and refined mesh can be positioned along the *Z*-axis as per the desired immersion depth.

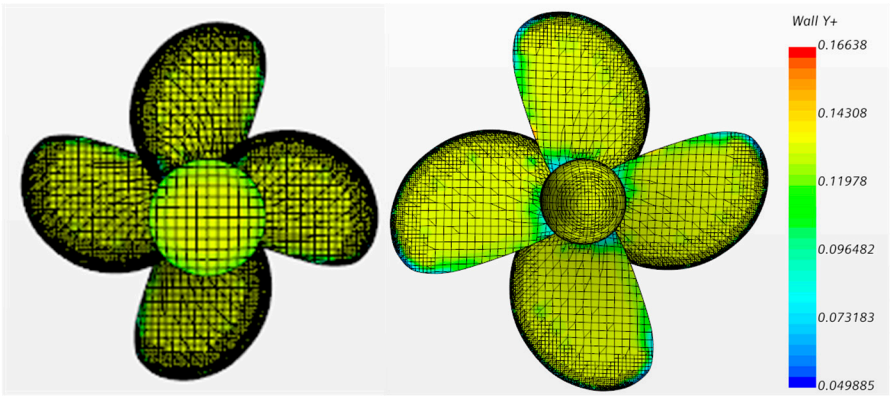

Figure 5. Wall Y+.

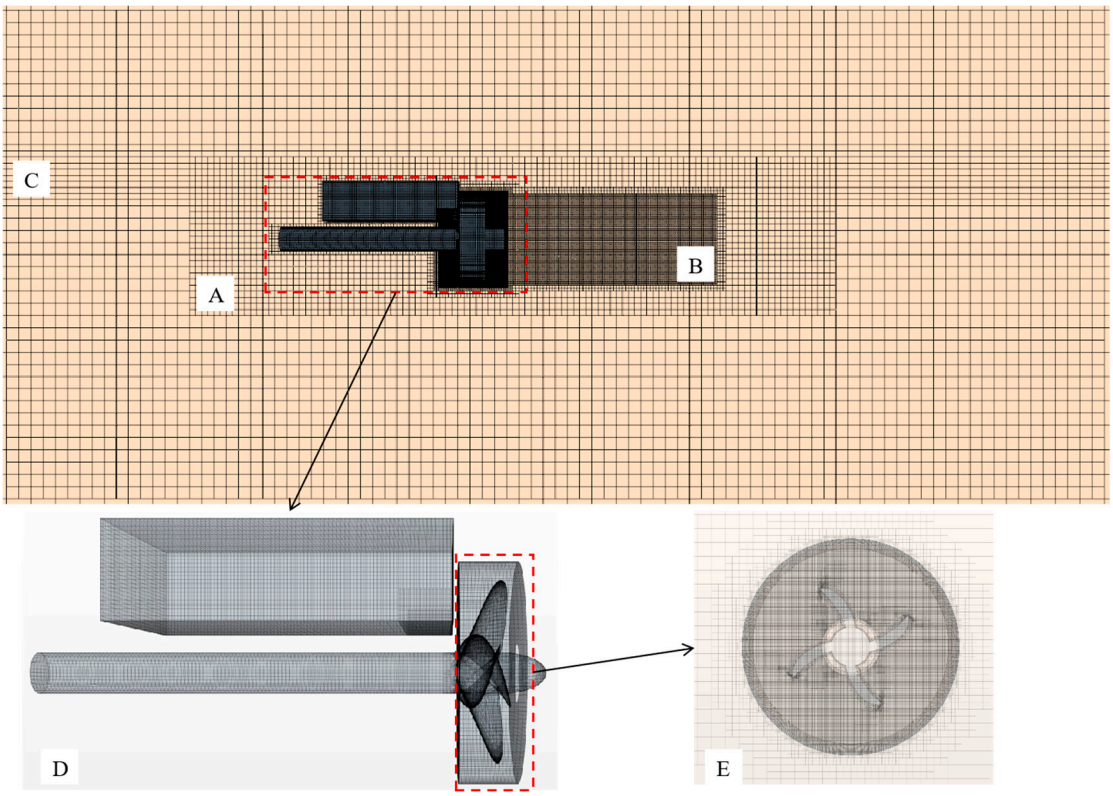

Figure 6. The computational domain grid. ((**A**,**B**) represent the refined mesh regions before and after the propeller, respectively, (**C**) denotes the refined mesh area at the waterline surface, (**D**) corresponds to the region containing the ice and propeller, (**E**) is the overlapping grid region).

3.3. Free Surface Simulation

The challenge in this numerical simulation lies in the impact of free surface fluctuations on the propeller cavitation. In this study, the VOF method was adopted to perform volume fraction weighting on the computational domain mesh, capturing the liquid and air separately through different weighting coefficients of the mesh. Figure 7 illustrates a cross-sectional view of the air-water interface. The upper part represents the air component, the lower part represents the liquid component, and the middle part is the air-water interface. The free surface takes into account the effects of wind, waves, and flow. A static water wave was set at the free surface, with the wave velocity matching the flow velocity.

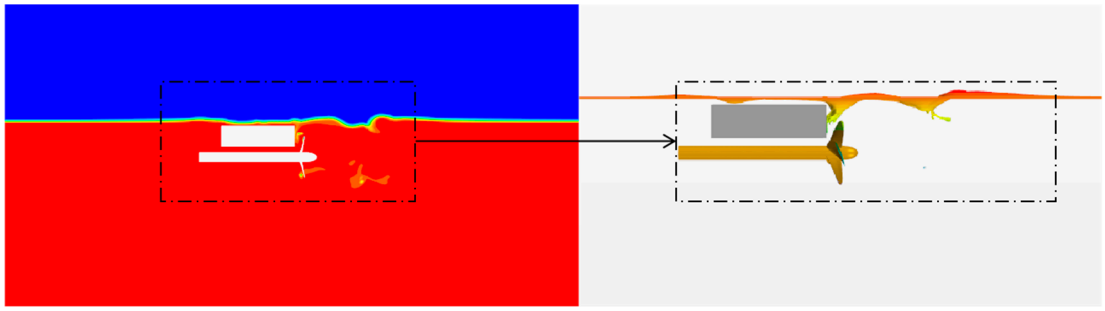

Figure 7. The free surface captured by the Volume of Fluid method.

The numerical simulation primarily investigates the effect of the free surface on the cavitation performance of an ice-blocked propeller at various immersion depths. To accurately predict the propeller cavitation performance at various immersion depths, the computational domain considers the effects of wind, waves, and flow. The saturation vapor pressure of water is established based on its value at room temperature; the reference pressure is set to the pressure at the corresponding cavitation number; the velocity is set to the speed of the still water wave; and the pressure is defined as the hydrostatic pressure. The numerical simulation is conducted in two stages. Initially, during the first stage, the propeller rotates to a stable state to obtain the propeller hydrodynamic performance at a stable rotation. In the second stage, the Schnerr-Sauer model for cavitation is introduced to determine the propeller cavitation performance at different immersion depths.

3.4. Study Cases

The immersion depth of the propeller refers to the vertical distance from the propeller shaft axis to the free surface. For the study of the cavitation performance of a propeller near the water surface, numerical simulations of the propeller were conducted at immersion depths ranging from 1 to 9D. The propeller cavitation performance was simulated both within the cavitation tunnel and near the water surface, and the results were compared with experimental data obtained from the cavitation tunnel. Regarding the numerical simulation near the water surface, the propeller cavitation performance was primarily studied based on the cavitation number, advance coefficient, and propeller immersion depth. In the numerical simulations, the propeller was operated at the rotational speed of 35 rps, and the spacing between ice and propeller was set at L/D = 0.15 [3]. Since both ice blockage and the free surface are major factors affecting the propeller cavitation performance, this paper primarily investigates the propeller cavitation performance at various immersion depths, cavitation numbers, and advance coefficients under specific ice blockage conditions. The specific research plan is outlined in Table 2.

Table 2. Study cases 1.

Operating Conditions	σ_n	J	Depth (H/D)
1	1.5	0.35	1, 2, 3, 4, 5, 6, 7, 8, 9

In the near-water surface region, the free surface has a significant impact on the propeller's hydrodynamic performance. However, when the propeller is immersed to a certain depth, the effect of the free surface can be negligible. Therefore, this paper simulated the propeller cavitation performance near the water surface and at a certain depth. The cases analyzed in this study are detailed in Table 3.

Table 3. Study cases 2.

Operating Conditions	σ_n	J	Depth (H/D)
1	1.5	0.35	1, 9
2	2.5	0.45	
3	3.5	0.55	
4	4.5	0.65	

4. Validation

4.1. Mesh Convergence Analysis

The mesh uncertainty analysis was performed according to ITTC [23]. In order to exclude the effect of Y+ and to ensure that the topological form of the boundary layer mesh remains the same, ITTC recommends a mesh refinement ratio of $2^{1/2}$ [24]. Based on the same mesh topology, three sets of meshes were generated by adjusting the mesh datum size. The coarse mesh count is 2.75 million, the medium mesh count is 3.89 million, and the fine mesh count is 5.5 million.

In the analysis of mesh convergence criteria, this paper compared the results of coarse meshes G^1_{coarse}, medium meshes G^2_{medium}, and fine meshes G^3_{fine} with those from cavitation tunnel experiments S_{test}, while also examining the numerical simulation difference across the three mesh types (D^1_S, D^2_S, D^3_S). The simulation results, as shown in Table 4, show that the numerical simulations under all three meshes exhibit differences of no more than 10% compared to the experimental results. The medium mesh employed in this study not only meets the required computational accuracy but also saves computational time, demonstrating its effectiveness in simulating the cavitation performance of the propeller.

Table 4. Three sets mesh parameters.

	G^1_{coarse}	G^2_{medium}	G^3_{fine}	S_{test}	D^1_S	D^2_S	D^3_S
K_T	0.235	0.246	0.261	0.247	−4.86%	−0.4%	5.67%
$10K_Q$	0.351	0.361	0.368	0.345	1.74%	4.64%	6.67%
η_0	0.48	0.489	0.508	0.512	−6.25%	−4.49%	−0.78%

4.2. Numerical Validation

The propeller cavitation characteristics in the uniform and the ice blockage conditions are investigated in the cavitation tunnel test at the China Research Center [3]. The ice blockage condition is when brash ice forms a blockage effect in front of the propeller. The brash ice model is simulated by a rectangular rigid body, and the propeller cavitation characteristics under ice blockage conditions with different distances between the ice and propeller, the cavitation number, and the advance coefficients.

The cavitation tunnel model experiments were carried out to validate the existing numerical models and to compare them with the propeller cavitation performance near the free surface. The numerical simulations primarily investigated the effects of the advance coefficient, cavitation number, and immersion depth on the propeller cavitation performance. The main parameters for validating the propeller are provided in Table 5. A snapshot of the propeller in the cavitation tunnel is shown in Figure 8, indicating that the cavitation phenomenon of the propeller was simulated and monitored effectively.

Table 5. Key propeller parameters [3].

Parameters	Full Scale	Model Scale
Scale λ	1	28
Diameter D (m)	7.0	0.25
Blades count Z	4	4
Pitch-to-diameter ratio of 0.7 R	0.84	0.84
Area ratio A_E/A_0	0.75	0.75
Hub-to-diameter ratio d_h/D	0.21	0.21

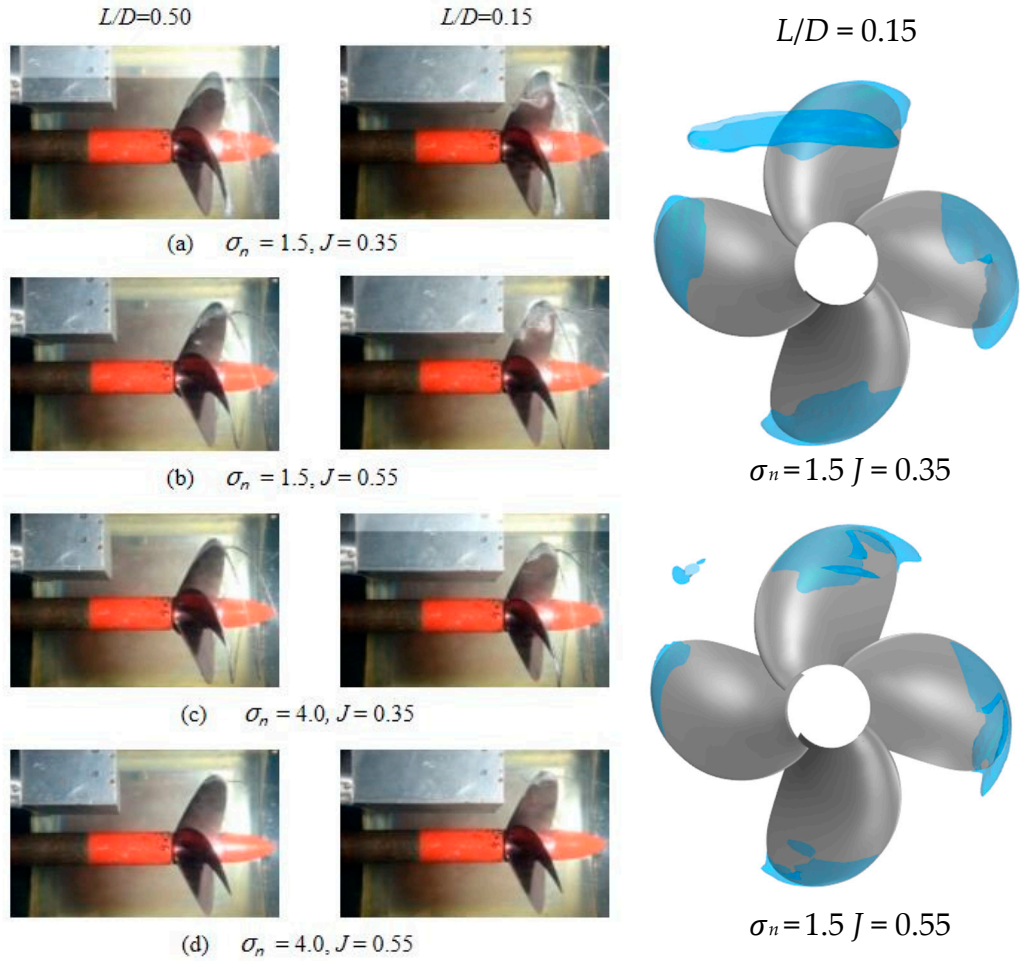

Figure 8. Snapshot of cavitation tunnel [3].

The cavitation tunnel experiments simulated propeller operation in an infinite water depth condition, with negligible consideration of the effect of the free surface. Furthermore, the cavitation tunnel experiments overlooked variations in liquid pressure at the propeller shaft. However, when ships navigate in brash ice channels, the ship-ice-propeller interaction generates fluctuations on the free surface. Free surface fluctuations can affect both the inflow in front of the propeller and the wake behind it. Moreover, variations in free surface fluctuations and pressure at the propeller shaft differ for ships navigated under various loaded conditions. Consequently, there exists a disparity between the cavitation tunnel experiments and the actual navigation conditions of ships. Nevertheless, when the propeller is immersed to a certain depth, the effect of the free surface can be disregarded. Through a continuous increase in the immersion depth, at 9D immersion depth, further increases do not significantly affect the propeller cavitation performance. Therefore, this paper concludes that at an immersion depth of 9D, the propeller cavitation performance is close to that of the cavitation tunnel.

Figure 9 shows a comparison between the experimental data from the cavitation tunnel [3], numerical simulation results from the cavitation tunnel, and numerical simulation results at an immersion depth of 9*D*. In this paper, the simulation condition of the cavitation tunnel is simulated by excluding the air phase when applying volume weighting to the computational grid using the Volume of Fluid method in the computational domain. At an immersion depth of 9*D*, the effect of the free surface is negligible. Therefore, the simulation condition of the cavitation tunnel and the propeller operating condition at an immersion depth of 9*D* can be compared with the cavitation tunnel model tests. The average differences between the simulated result K_{T0}, $10K_{Q0}$, η_0, and the experimental data K_T, $10K_Q$, η in the cavitation tunnel are 3.8%, 1.69%, and 0.59%, respectively. At an immersion depth of 9*D*, the average difference between the simulated result K_{T1}, $10K_{Q1}$, η_1 and the experimental data K_T, $10K_Q$, η in the cavitation tunnel are 0.69%, 3.71%, and 3.32%, respectively. There is no apparent trend in the changes in the propeller thrust coefficient and torque coefficient relative to the experimental data. Although the cavitation tunnel neglects the effect of the free surface, the liquid pressure within the cavitation tunnel is significantly lower compared to an infinite water depth. Consequently, as the advance coefficient increases, the flow velocity within the flow field increases. The effect of flow velocity on the pressure of the propeller blades outweighs the effect of liquid pressure. However, at an immersion depth of 9*D*, the impact of liquid pressure on the pressure of the propeller blades is more substantial than that of flow velocity. Thus, the two curve trends depicted in the figure below occur.

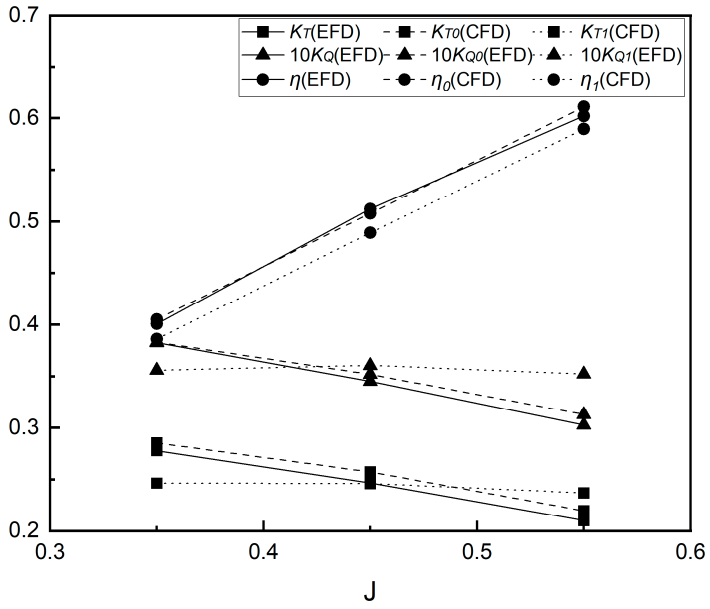

Figure 9. Comparison of mean propeller cavitation performance between the numerical results of the simulation condition of the cavitation tunnel (K_{T0}, $10K_{Q0}$, η_0, CFD), the numerical results of the propeller operating condition at an immersion depth of 9D (K_{T1}, $10K_{Q1}$, η_1, CFD, CFD), and the cavitation tunnel model test results (K_T, $10K_Q$, η, EFD).

5. Results and Analysis

5.1. Cavitation Performance for Different Immersion Depths

To analyze the propeller cavitation performance at different immersion depths, nine immersion depths were selected based on the positioning of the computational domain along the *z*-axis. The simulated result for the propeller at various immersion depths is illustrated in Figure 10, with each result point labeled using symbols. Non-linear fitting was employed for the simulation results, with the fitted curve represented as the quadratic fit to the simulated result. The fitted curves illustrate the variation patterns of propeller thrust, torque, and efficiency with immersion depth, which led to the classification of the study

cases into two groups. Study case 1 pertains to the investigation of the regularity curves. Study case 2 pertains to the investigation of typical working conditions, with simulated results closely aligning with the regularity curves. The arrangement of the study cases significantly saved computation time.

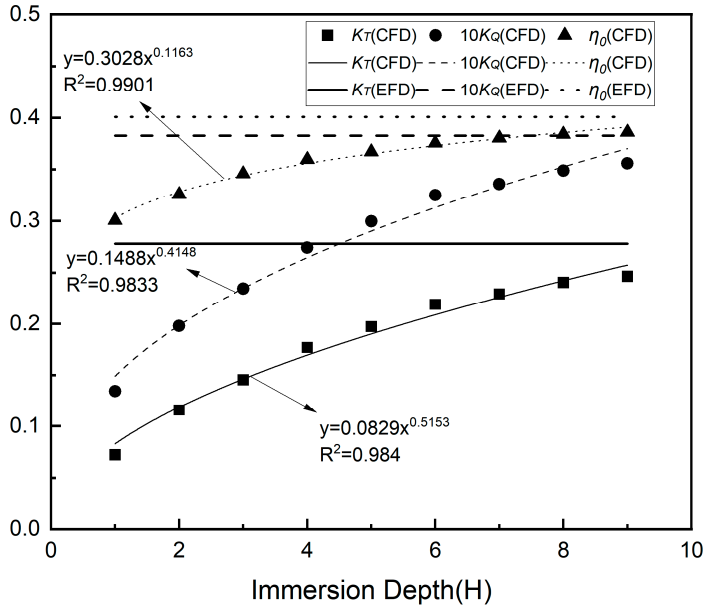

Figure 10. Comparison of experimental and simulated results.

During the simulation process, considering the effect of initial water surface fluctuations upon the initial rotation of the propeller, approximately 0.2 s were required for the propeller to reach a stable rotation. The simulation result represents the average values from 0.3 to 0.5 s of propeller operation. As the immersion depth increases, the trends for the propeller thrust coefficient, torque coefficient, and propeller efficiency tend to stabilize. When $J = 0.35$, $L/D = 0.15$ and $\sigma_n = 1.5$, the average thrust and torque of the propeller at various immersion depths were simulated. Table 6 presents the propeller thrust coefficient K_T, torque coefficient $10K_Q$, and propeller efficiency η under different conditions. At an immersion depth of $1D$, the propeller thrust coefficient and torque coefficient under ice-blocked conditions were approximately one-fourth of those at an infinite water depth, with a 20% decrease in propeller efficiency. At an immersion depth of $9D$, the discrepancies in the propeller thrust coefficient, torque coefficient, and propeller efficiency from the experimental data were within 10%.

Table 6. Numerical and experiment data analysis.

Operation Conditions	K_T	$10K_Q$	η_0
Cavitation tunnel	0.2778	0.3825	0.4006
$1D$	0.0724	0.1342	0.3006
$9D$	0.2501	0.3558	0.3859

Brash ice restricts the maneuverability of ships and affects the propeller hydrodynamic performance through collisions, compression, and blockage [24]. At an immersion depth of $1D$, the propeller hydrodynamic performance is the worst. Therefore, this paper primarily investigated the propeller hydrodynamic performance at an immersion depth of $1D$. Figure 11 represents the propeller open-water performance at an immersion depth of $1D$. In the near-water surface region, when propeller cavitation is not considered, the trends in propeller thrust coefficient, torque coefficient, and propeller efficiency are similar to those observed in the cavitation tunnel experiment. The propeller open-water performance

refers to the operating condition without considering cavitation. However, the propeller cavitation is inevitable. In the near-water surface region, the fluctuation of the free surface significantly affects the cavitation of the propeller. Therefore, the propeller cavitation performance near the free surface is of significant research interest.

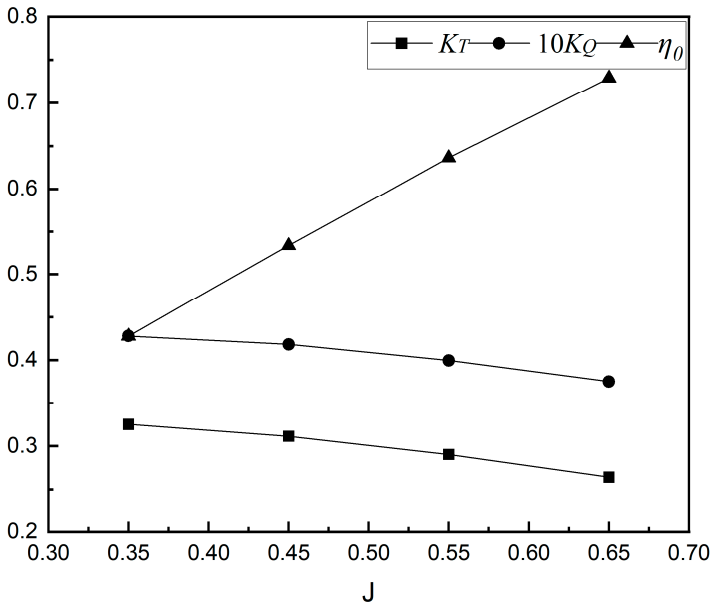

Figure 11. Propeller open-water performance at an immersion depth of 1D under various advance coefficients *J*.

To investigate the propeller cavitation performance near the free surface, this paper conducted propeller cavitation simulations for different advance coefficients and cavitation numbers. Figure 12 illustrates the propeller cavitation simulation result at an immersion depth of 1*D*. High-speed rotation of the propeller near the water surface generates significant turbulence and wave resistance, which increases with the flow velocity. Compared to the cavitation tunnel experiments, the propeller cavitation performance near the free surface is primarily affected by the free surface fluctuations. As the advance coefficient increases, the inflow velocity ahead of the propeller relative to its rotational speed also increases, resulting in a higher propulsive force. Consequently, the propeller thrust coefficient, torque coefficient, and propeller efficiency exhibit an increasing trend. In the numerical simulations, the cavitation number is determined based on the pressure in the computational domain, the saturation vapor pressure of water, and the pressure at the propeller shaft center at the current depth. As the cavitation number increases, the pressure within the flow field rises, reducing the area of low pressure on the blade surface and making it difficult for cavitation to attach. The propeller thrust coefficient, torque coefficient, and propeller efficiency all increase.

To confirm the negligible effect of the free surface at a specific immersion depth, simulations of propeller cavitation were carried out for various advance coefficients at a propeller immersion depth of 9*D*. Figure 13 represents the cavitation simulation data for the propeller at various cavitation numbers. At an immersion depth of 9*D*, as the advance coefficient *J* increases, the propeller thrust coefficient and torque coefficient exhibit a decreasing trend, while the propeller efficiency shows a linear upward trend. This trend aligns with the results obtained from the cavitation tunnel experiments.

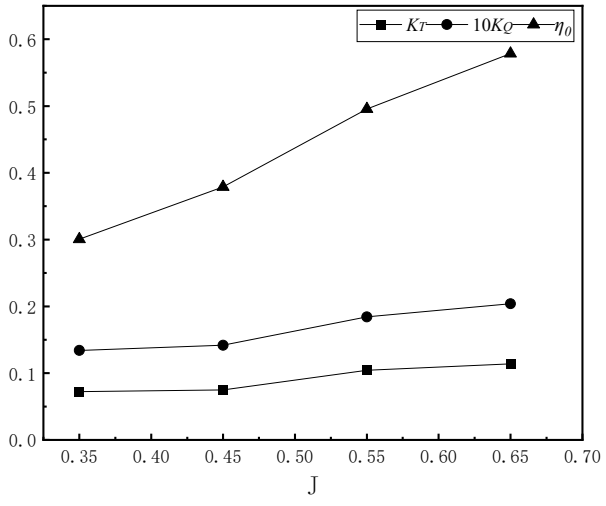

(**A**)

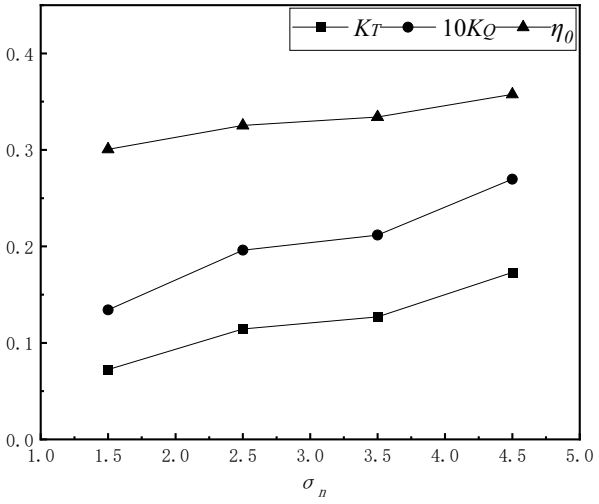

(**B**)

Figure 12. Propeller cavitation performance at an immersion depth of 1*D*. (**A**) Propeller cavitation performance under various advance coefficients *J*. (**B**) Propeller cavitation performance under various cavitation numbers σ_n.

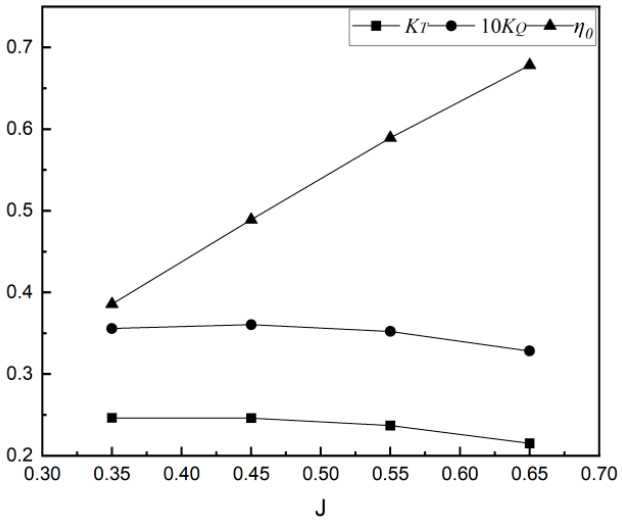

Figure 13. Propeller cavitation performance at various advance coefficients *J*.

5.2. Cavitation Phenomenon and Pressure Distribution

To further investigate the propeller cavitation performance, this paper studied the cavitation shape and pressure distribution of the propeller at different immersion depths, cavitation numbers, and advance coefficients. The most severe cavitation case of the propeller at a specific moment was monitored. An analysis of the pressure distribution on the propeller blades was also conducted. The pressure coefficient is defined by the following equation:

$$C_p = \frac{P - P_0}{\rho(nD)^2} \tag{12}$$

where P is the pressure of the shaft center, P_0 is the pressure of domain, and n represents the propeller rotational speed.

Figures 14 and 15 illustrate the cavitation phenomenon and blade pressure distribution of the propeller at an immersion depth of $1D$. From the figure, it can be observed that at $J = 0.35$ and $\sigma_n = 1.5$, the propeller is fully covered by cavitation, and the blade pressure coefficients are all below 0. At high rotational speeds, the cavitation patterns on the propeller blades vary at each moment, reflecting the cavitation collapse process on the propeller. With an increase in flow velocity in the vicinity of the water surface, the wave resistance exerted on the propeller blades by the fluctuating free surface becomes more significant. The cavitation on the propeller blades is highly unstable, and the process from cavitation generation to collapse occurs in an instant. Furthermore, as the advance coefficient and cavitation number increase, the pressure coefficients on the suction side of the propeller blades gradually increase from the root to become positive values. The low-pressure region on the blades decreases, making it difficult for cavitation to adhere to the propeller blades.

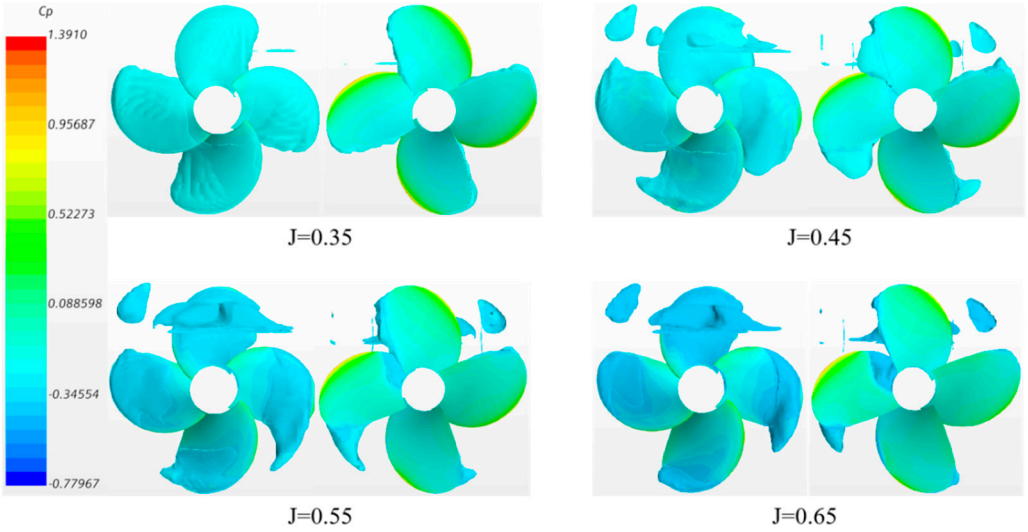

Figure 14. Variation of cavitation phenomena with advance coefficient.

To investigate the effect of immersion depth on the propeller cavitation performance, this paper monitored and analyzed the cavitation phenomena under different immersion depths. Figures 16 and 17 illustrate the propeller cavitation phenomenon and the pressure distribution on the blade surface at different immersion depths. When the propeller immersion depth ranges from 1 to $3D$, the water surface fluctuations have a significant impact on the propeller cavitation, with cavitation observed near the blades. Additionally, the propeller blades are almost entirely covered by cavitation. As the immersion depth increases from 3 to $9D$, the effect of the free surface on the propeller cavitation gradually diminishes. At an immersion depth of $9D$, the propeller cavitation phenomenon aligns well with the experimental observations. The pressure on the blade surface shows an increasing trend with the rise in immersion depth, with the maximum pressure coefficient occurring

between 0.6R and 1.0R. In the low-pressure region, the pressure coefficient on the suction side of the propeller blade is less than 0. As the immersion depth increases, the pressure on the surface of the blade also increases, which makes it challenging for cavitation to attach to the blade surface. Sheet cavitation transitions into cloud cavitation, while tip vortex cavitation significantly increases.

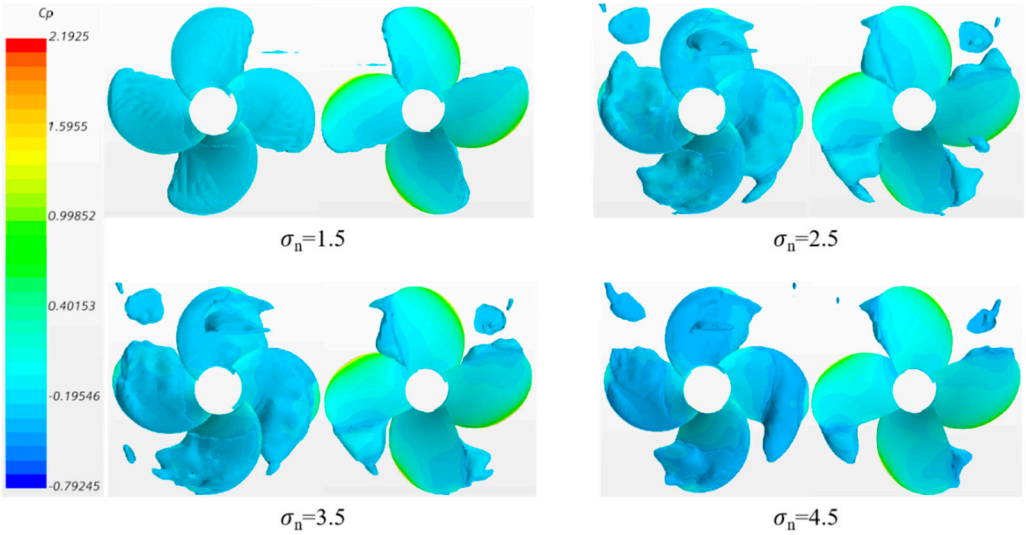

Figure 15. Variation of cavitation phenomena with cavitation number.

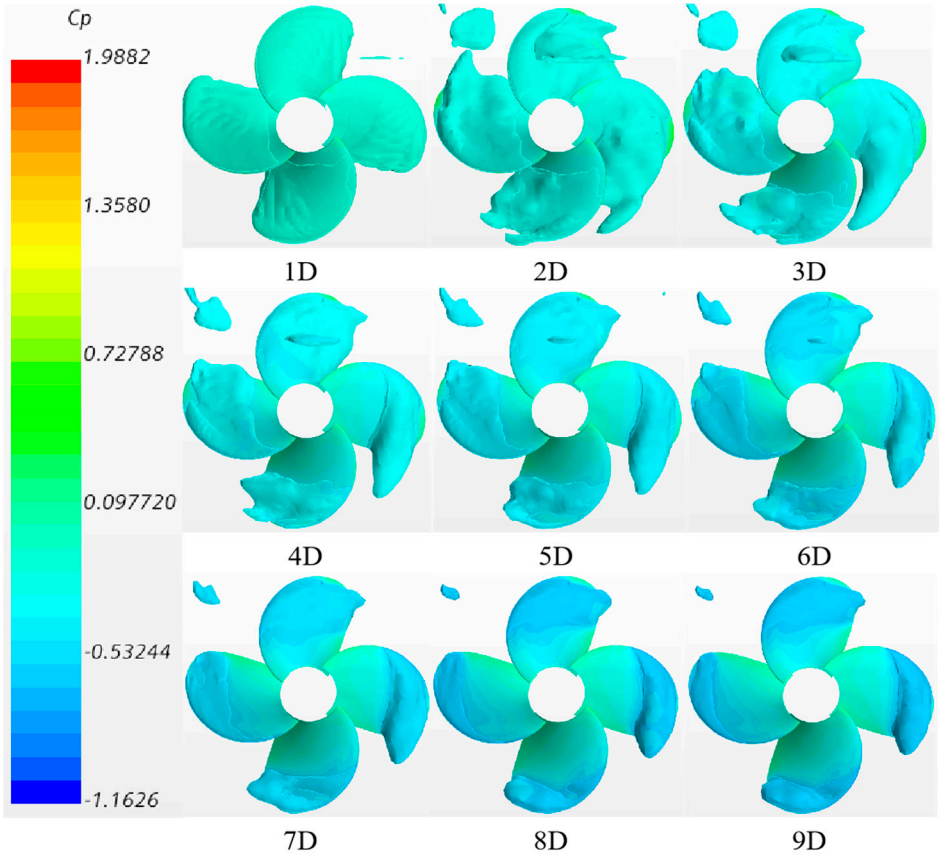

Figure 16. Variation of pressure coefficient on suction side.

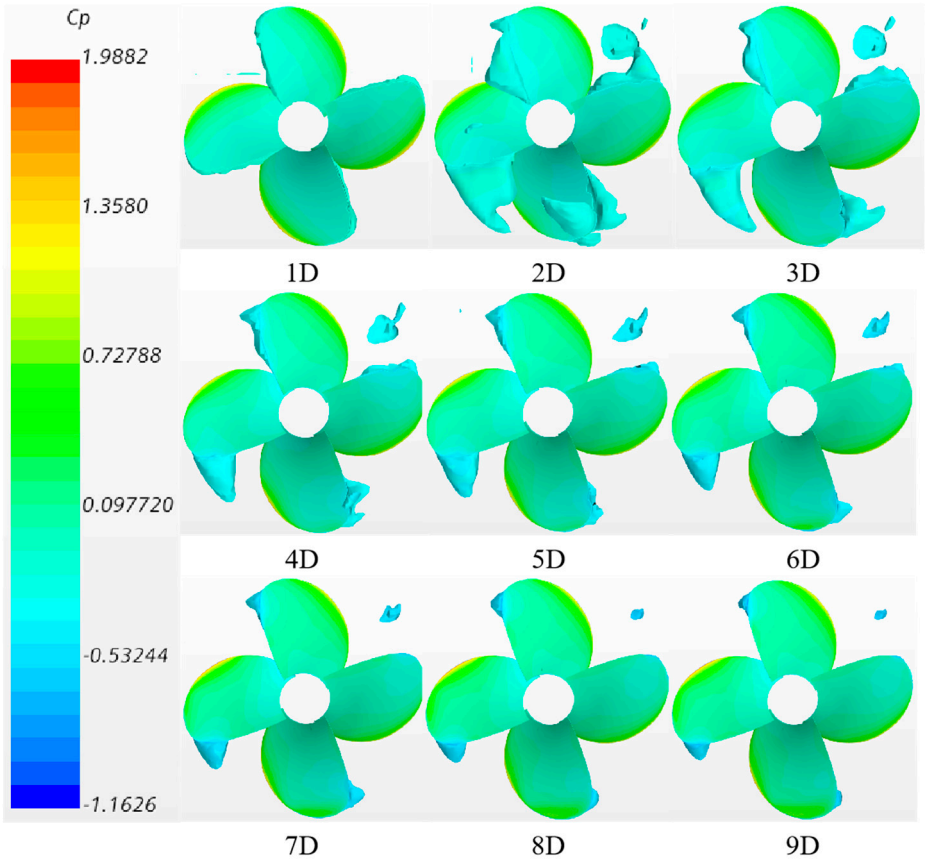

Figure 17. Variation of pressure coefficient on pressure side.

The generation, development, and collapse of cavitation constitute the cavitation phenomenon. Cavitation is a continuous and transient process, which requires the propeller to reach a steady-state imported cavitation model to accurately capture the cavitation phenomenon. To investigate the impact of the introduction of the cavitation model on the stable state of the propeller with the presence of the free surface, this paper analyzed the historical curves of the thrust and torque of the propeller.

Figure 18 illustrates the historical curves of the thrust and torque of the propeller, with a time step set at 0.0005s, which required 57.1 steps for one complete revolution of the propeller. The first stage involves the propeller rotating from a stationary state to a stable one, while the second stage involves the direct introduction of the Schnerr-Sauer cavitation model. Directly incorporating the propeller thrust and torque results in an instant drop followed by a rise until a stable buffering phase is reached. In contrast to the cavitation tunnel experiment, during the second stage, the propeller is affected by cavitation, the free surface, and ice blockage simultaneously, leading to highly unstable propeller thrust and torque. At an immersion depth of 1D, the historical curves show prolonged fluctuations after the introduction of the cavitation model. The propeller thrust and torque decreased to approximately one-fourth of their original values. At an immersion depth of 9D, the historical curves exhibit minimal fluctuations after the introduction of the cavitation model, and the propeller quickly reaches a stable state. Thus, in the near-water surface region, the fluctuation of the free surface is a significant factor in the propeller cavitation performance.

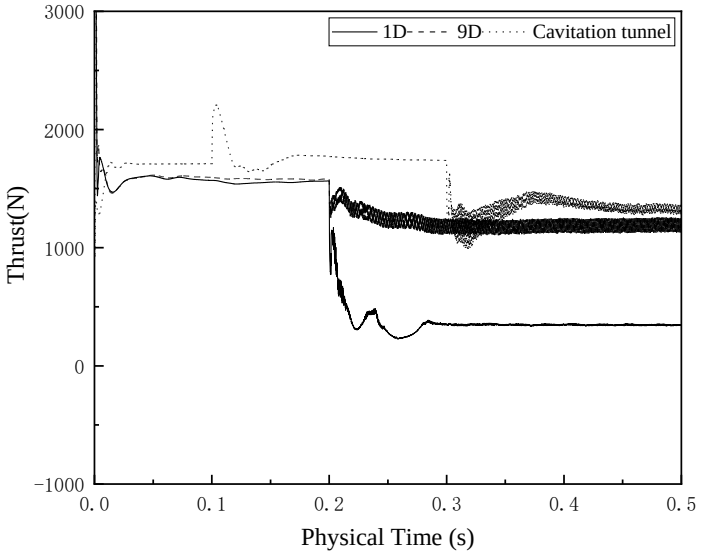

(**A**)

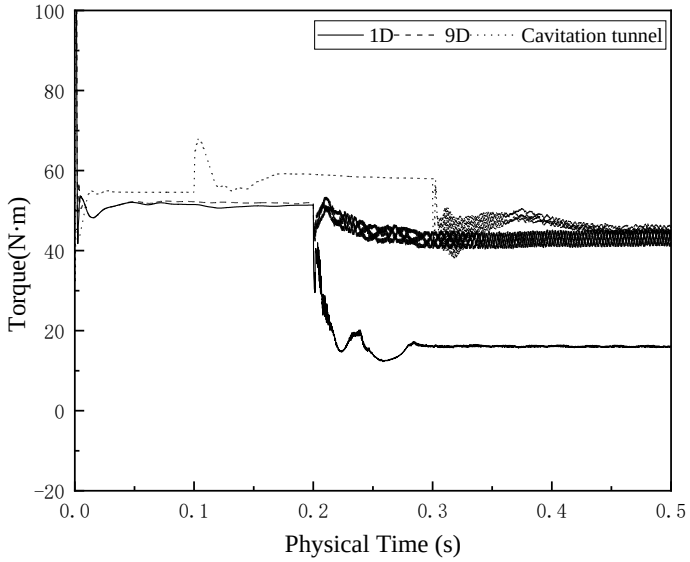

(**B**)

Figure 18. Time history of thrust and torque for the propeller under various computational conditions. (**A**) Time history of thrust for the propeller. (**B**) Time history of torque for the propeller.

5.3. Cavitation Excitation Forces

To investigate the effect of free surface fluctuations on the cavitation excitation forces of the propeller, this paper monitored the propeller thrust and torque at various immersion depths. Additionally, the data were transformed into the frequency domain using fast Fourier transformation to facilitate comparative analysis. Figures 19 and 20 show the thrust and torque fluctuations of the propeller at various immersion depths. As mentioned earlier, when the propeller is at an immersion depth of 1D, the propeller surface is completely covered by cavitation. The high-amplitude region and vibration frequency of the propeller are concentrated at low frequencies. As the immersion depth increases, the high-amplitude region and vibration frequency shift to the mid-low frequency range. However, the amplitudes of thrust and torque decrease continuously, and the vibration frequency of the propeller blades remains relatively stable. The cavitation around the propeller reduces. Consequently, the propeller achieves relatively high propulsion efficiency at a certain immersion depth.

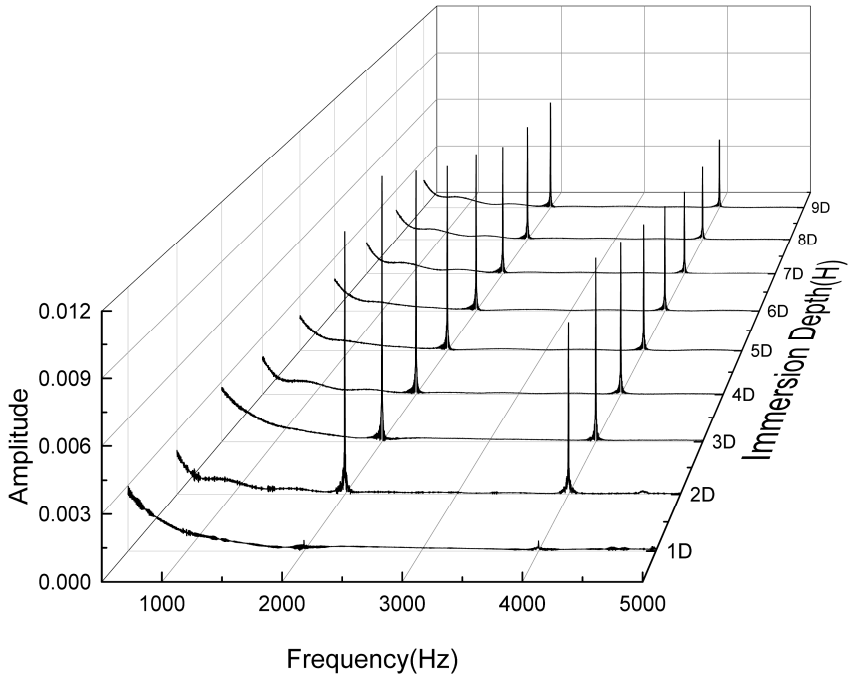

Figure 19. Frequency spectrum analysis of thrust pulsation of propellers at immersion depths of 1–9*D*.

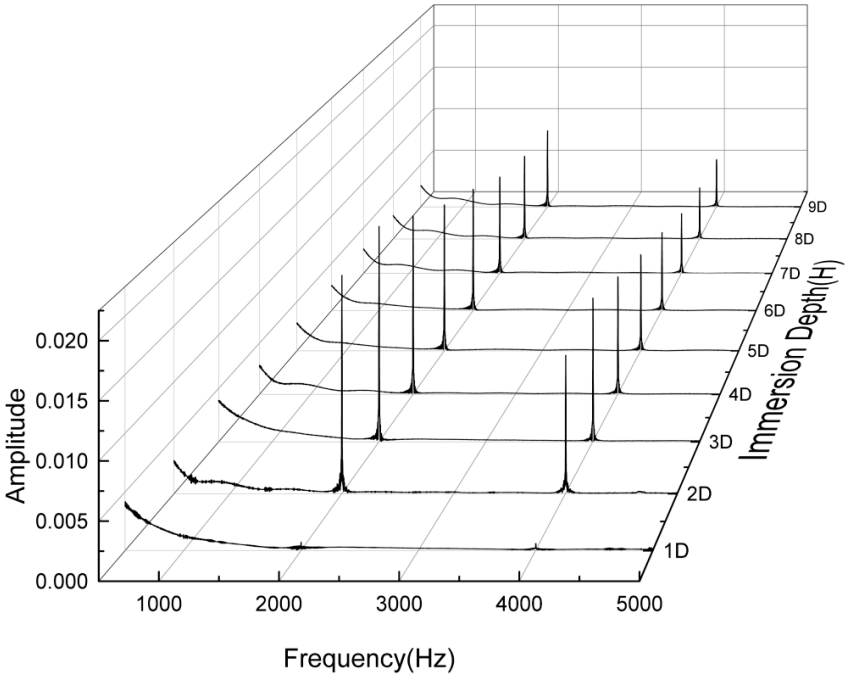

Figure 20. Frequency spectrum analysis of torque pulsation of propellers at immersion depths of 1–9*D*.

Considering the poor propeller hydrodynamic performance near the free surface, this paper analyzed the thrust and torque fluctuations of the propeller under different advance coefficients and cavitation numbers to investigate the factors contributing to the deterioration of the propeller hydrodynamic performance. During the rotation of the propeller, the formation and collapse of cavitation cause rapid pressure fluctuations around the blades. These cavitation excitation forces contribute to the instability of the surrounding flow field, which is a key factor driving the vibrations in thrust and torque.

Figures 21–24 illustrate how the curve of cavitation excitation forces varied with the advance coefficient and cavitation number. When operated near the free surface, the

propeller exhibits significant low-frequency vibrations with relatively small amplitudes. The parts with larger amplitudes are mainly concentrated in the mid-frequency vibration range. As the advance coefficient and cavitation number increase, the propeller thrust and torque vibrations become more pronounced, with little change in the amplitude. When J = 0.35 and σ_n = 1.5, the propeller blades are completely covered by cavitation. The propeller exhibits significant vibration amplitude at low frequencies, and cavitation phenomena are mostly associated with low-frequency vibrations. As the advance coefficient and cavitation number increase, the cavitation phenomenon weakens, and the propeller blades begin to exhibit medium- to high-frequency vibrations. Therefore, with an increase in the propeller blade pressure, the vibration frequency of the propeller blade also increases.

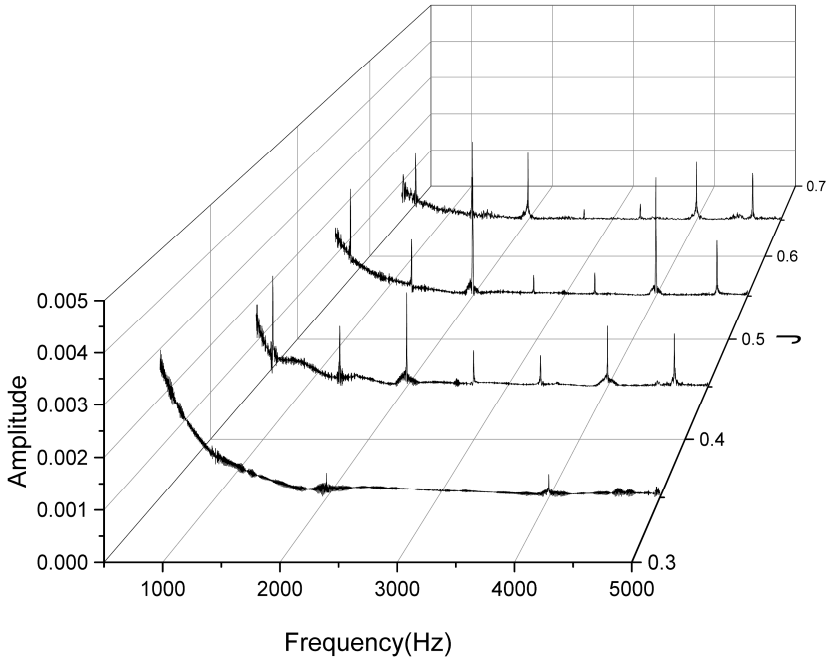

Figure 21. Frequency spectrum analysis of thrust pulsation under variations of advance coefficient.

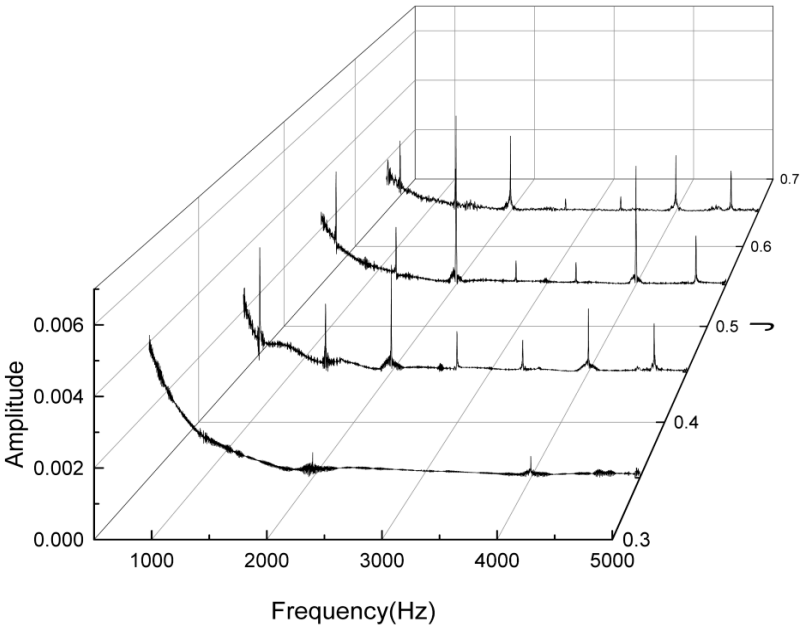

Figure 22. Frequency spectrum analysis of torque pulsation under variations of advance coefficient.

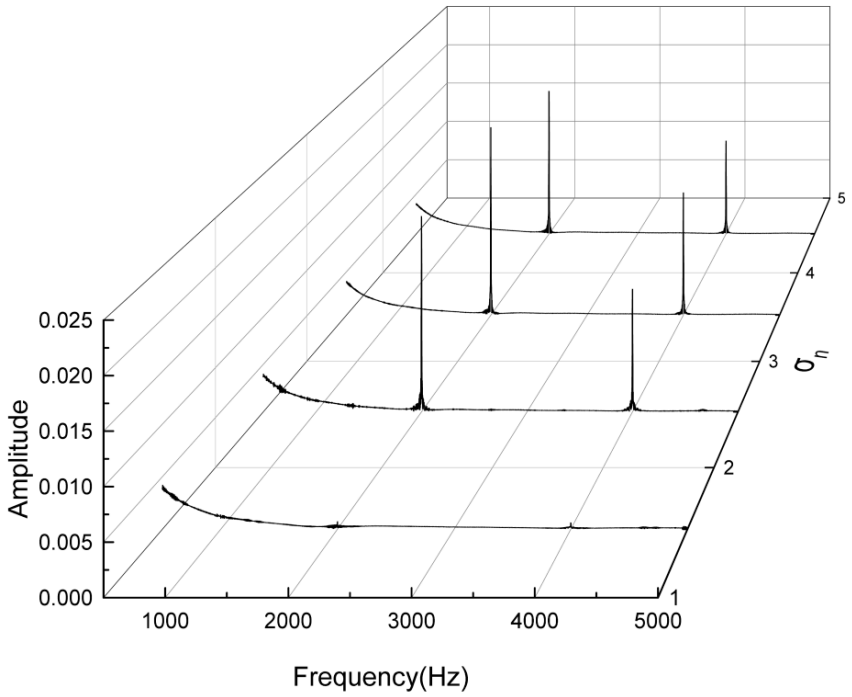

Figure 23. Frequency spectrum analysis of thrust pulsation under variations of cavitation number.

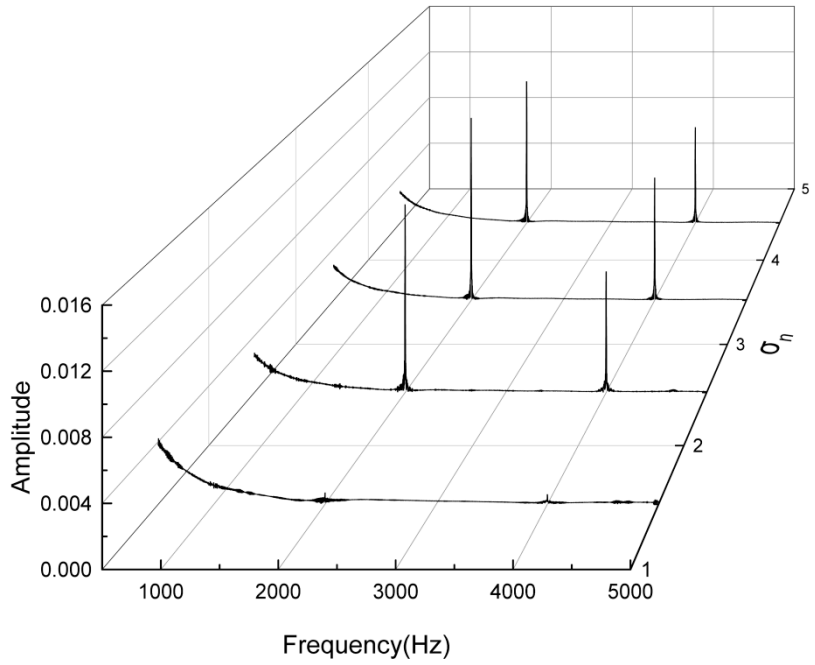

Figure 24. Frequency spectrum analysis of torque pulsation under variations of cavitation number.

5.4. Vortex Intensity

Based on the cavitation phenomena of the propeller at an immersion depth of 1*D*, this paper primarily analyzed the blade vortex intensity of the propeller under different cavitation numbers and advance coefficients. The vortex intensity distribution on the suction and pressure sides of the blades at the moment when the propeller experiences the most severe cavitation was examined. Figures 25 and 26 illustrate the distribution of vortex intensity on the suction and pressure sides of the propeller blades. A low-pressure center exists in the vortex intensity on the suction side of the propeller, while the vortex intensity is systematically distributed on the pressure side of the propeller blades. The maximum

and minimum vortex intensity occur at the blade tip and root, respectively. As the advance coefficient and cavitation number increased, the attachment of cavitation at the blade tip on the suction side diminished the contact area between the viscous water and the blade, leading to a reduction in vortex intensity. The decrease in the area of low-pressure and cavitation coverage on the suction side corresponds to a similar trend in vortex intensity. The vortex intensity on the pressure side of the propeller gradually diminishes.

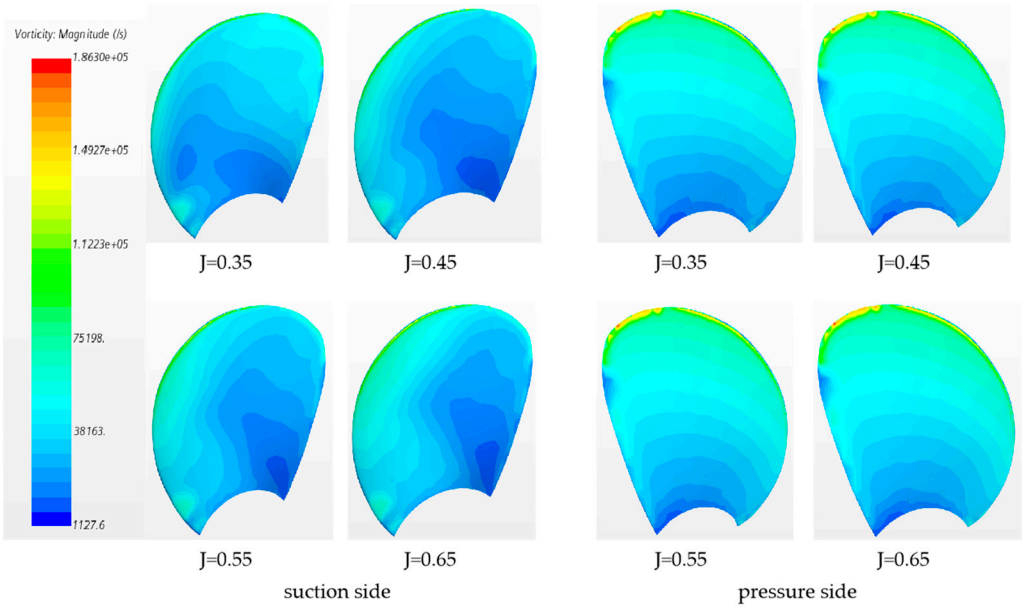

Figure 25. Variation of vortex intensity with advance coefficient.

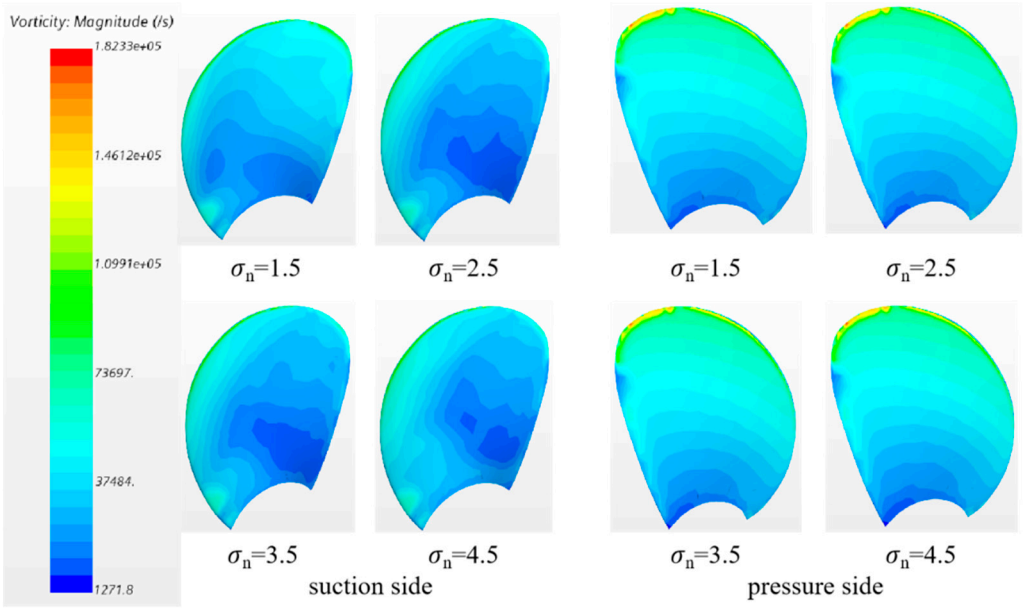

Figure 26. Variation of vortex intensity with cavitation number.

6. Conclusions

This paper employed a CFD-VOF coupled method based on RANS and the overlapping grid technique in conjunction with experimental investigations in a cavitation tunnel. The study focused on the propeller cavitation performance in ice blockage conditions at various immersion depths. From the experimental and numerical simulation results, the following conclusions were established:

(1) The computational grid of the numerical model can be positioned along the *Z*-axis to compute the propeller cavitation performance at different immersion depths. The numerical simulation results closely align with the experimental data from the cavitation tunnel, with the difference within 5%.
(2) When cavitation is not taken into account, the thrust and torque coefficients of the propeller show a consistent decrease, which corresponds with the results observed in cavitation tunnel experiments. Conversely, when the cavitation model is introduced, the presence of the free surface results in a gradual increase in both the thrust and torque coefficients. Furthermore, the free surface contributes to a decline in the cavitation performance of the propeller by over 10%.
(3) When σ_n = 1.5 and L/D = 0.15, the cavitation area of the propeller diminishes as the immersion depth, cavitation number, and advance coefficient increase, aligning with the results observed in cavitation tunnel experiments. Notably, immersion depth and advance coefficient exert a more significant effect on the cavitation area than the cavitation number, with reductions exceeding 50%.
(4) Cavitation excitation forces play a crucial role in the vibrations of the propeller. As the immersion depth decreases, the amplitudes of thrust and torque rise. When operating near the free surface, the vortex intensity on the suction side of the propeller is markedly greater than that on the pressure side due to these vibrations. Notably, a region of elevated vortex intensity forms along the tip of the suction side.

It should be noted that the numerical simulation approach in this study does not consider the effect of the ship hull and ship-ice interactions on the propeller inflow field. There may be some discrepancies between the simulation results and the actual conditions. Future research will concentrate on simulating the cavitation performance of propellers located at the stern of the ship. This study will assess cavitation performance across different ice-breaking conditions in brash ice channels while considering the effects of the ship and the free surface. Future work is to simulate the cavitation performance of propellers located aft of the ship and consider the effect of ship-ice interactions on the free surface. This is important for the design and manufacture of ice-class propellers.

Author Contributions: L.Z.: Investigation, Formal analysis, Writing—review and editing, Supervision, Project administration, Funding acquisition. A.Z.: Conceptualization, Methodology, Software, Investigation, Formal analysis, Writing original draft. S.D.: Formal analysis, Writing—review and editing. S.H.: Formal analysis, Writing—review and editing. F.L.: Formal analysis, Writing—review and editing, Funding acquisition. P.K.: Formal analysis, Writing—review and editing. All authors have read and agreed to the published version of the manuscript.

Funding: This work is supported by the National Key Technologies Research and Development Program (Grant No. 2022YFE0107000), General Projects of National Natural Science Foundation of China (Grant No. 52171259), and High-tech ship research project of Ministry of Industry and Information Technology ([2021]342), CSSC-SJTU joint prospect funding (ZCJDQZ202307A01), and Science and Technology Commission of Shanghai Municipality Project (22DZ1204403, 23YF1419900), Foundation of State Key Laboratory of Ocean Engineering in Shanghai Jiao Tong University (GKZD010086-2), Young Scientists Fund of National Natural Science Foundation of China (52301331).

Data Availability Statement: Data are contained within the article.

Conflicts of Interest: The authors declare that they have no conflict of interest.

References

1. Zhu, Z.-F.; Fang, S.-L.; Wang, X.-Y.; Meng, Z.-W.; Liu, P.-X.; Du, X.-M. Numerical simulation of viscous cavitating flow around a ship propeller. *China Ocean Eng.* **2011**, *25*, 539–548. [CrossRef]
2. Sun, Q.; Chen, J.; Zhou, L.; Ding, S.; Han, S. A study on ice resistance prediction based on deep learning data generation method. *Ocean Eng.* **2024**, *301*, 117467. [CrossRef]
3. Zhou, L.; Zheng, S.; Diao, F.; Ding, S.; Gao, J. Experimental and numerical study on ice blockage performance of propeller in cavitation flow. *Water* **2022**, *14*, 1060. [CrossRef]

4. Zhou, L.; Zheng, S.; Ding, S.; Xie, C.; Liu, R. Influence of propeller on brash ice loads and pressure fluctuation for a reversing polar ship. *Ocean Eng.* **2023**, *280*, 114624. [CrossRef]
5. Ebrahimi, A.; Razaghian, A.; Tootian, A.; Seif, M. An experimental investigation of hydrodynamic performance, cavitation, and noise of a normal skew B-series marine propeller in the cavitation tunnel. *Ocean Eng.* **2021**, *238*, 109739. [CrossRef]
6. Khan, A.G.; Hisette, Q.; Streckwall, H.; Liu, P. Numerical investigation of propeller-ice interaction effects. *Ocean Eng.* **2020**, *216*, 107716. [CrossRef]
7. Viitanen, V.; Sipilä, T.; Sánchez-Caja, A.; Siikonen, T. CFD predictions of unsteady cavitation for a marine propeller in oblique inflow. *Ocean Eng.* **2022**, *266*, 112596. [CrossRef]
8. Baek, D.-G.; Yoon, H.-S.; Jung, J.-H.; Kim, K.-S.; Paik, B.-G. Effects of the advance ratio on the evolution of a propeller wake. *Comput. Fluids* **2015**, *118*, 32–43. [CrossRef]
9. Meng, C.-L.; Dong, L.-Y.; Wang, D.-H.; He, J.-X.; Shuai, Z.-J.; Li, W.-Y.; Ni, S.-W.; Jiang, C.-X. Propeller hydrodynamic excitation influenced by shafting whirling vibration considering different nonuniform inflow conditions: A numerical study. *Ocean Eng.* **2023**, *288*, 116021. [CrossRef]
10. Hou, L.; Hu, A. Theoretical investigation about the hydrodynamic performance of propeller in oblique flow. *Int. J. Nav. Archit. Ocean Eng.* **2019**, *11*, 119–130. [CrossRef]
11. Guo, C.-y.; Zhao, D.-g.; Sun, Y. Numerical simulation and experimental research on hydrodynamic performance of propeller with varying shaft depths. *China Ocean Eng.* **2014**, *28*, 271–282. [CrossRef]
12. Califano, A.; Steen, S. Numerical simulations of a fully submerged propeller subject to ventilation. *Ocean Eng.* **2011**, *38*, 1582–1599. [CrossRef]
13. Tokgoz, E.; Wu, P.-C.; Takasu, S.; Toda, Y. Computation and experiment of propeller thrust fluctuation in waves for propeller open water condition. *Proc. Jpn. Soc. Mar. Mar. Eng.* **2017**, *25*, 55–62. [CrossRef]
14. Chen, Y.-W.; Pan, C.-C.; Lin, Y.-H.; Shih, C.-F.; Shen, J.-H.; Chang, C.-M. Acoustic Field Radiation Prediction and Verification of Underwater Vehicles under a Free Surface. *J. Mar. Sci. Eng.* **2023**, *11*, 1940. [CrossRef]
15. Jin, Z.; Wang, P.; Dong, H.; An, X.; Xia, H. Numerical prediction of ducted propeller performance based on a BEM–RANS coupling method. *Ocean Eng.* **2023**, *271*, 113761. [CrossRef]
16. Liu, Z.-h.; Wang, B.-l.; Peng, X.-x.; Liu, D.-c. Calculation of tip vortex cavitation flows around three-dimensional hydrofoils and propellers using a nonlinear k-ϵ turbulence model. *J. Hydrodyn. Ser. B* **2016**, *28*, 227–237. [CrossRef]
17. Zhang, G.; Yao, J. Numerical analysis of propeller hydrodynamic performance in waves. *J. Shanghai Jiao Tong Univ.* **2024**, *58*, 175–187.
18. Hirt, C.W.; Nichols, B.D. Volume of fluid (VOF) method for the dynamics of free boundaries. *J. Comput. Phys.* **1981**, *39*, 201–225. [CrossRef]
19. Zha, J. Numerical Wavemaking and Wave Dissipation Modeling Based on OpenFOAM and Its Application. Master's Thesis, Shanghai Jiaotong University, Shanghai, China, 2011.
20. Boswell, R.J. *Design, Cavitation Performance, and Open-Water Performance of a Series of Research Skewed Propellers*; Department of the Navy, Naval Ship Research and Development Center: Monterey, CA, USA, 1971.
21. Zhou, L.; Sun, Q.; Ding, S.; Han, S.; Wang, A. A machine-learning-based method for ship propulsion power prediction in ice. *J. Mar. Sci. Eng.* **2023**, *11*, 1381. [CrossRef]
22. Liang, B.; Wang, M.; Zhang, Q.; Yang, F.; Qin, Y.; Wang, X.; Wang, Z. Performance and wake flow of non/ducted-propeller in interaction with a downstream wall. *Ocean Eng.* **2024**, *304*, 117628. [CrossRef]
23. ITTC. Recommended Procedure and Guidelines, Uncertainty analysis in CFD verification and validation—Methodology and validation. In Proceedings of the 28th International Towing Tank Conference, Wuxi, China, 17–22 September 2017.
24. Li, F.; Chen, J.; Zhou, L.; Kujala, P. Investigation of ice wedge bearing capacity based on an anisotropic beam analogy. *Ocean Eng.* **2024**, *302*, 117611. [CrossRef]

Disclaimer/Publisher's Note: The statements, opinions and data contained in all publications are solely those of the individual author(s) and contributor(s) and not of MDPI and/or the editor(s). MDPI and/or the editor(s) disclaim responsibility for any injury to people or property resulting from any ideas, methods, instructions or products referred to in the content.